MDPI

Article

Laser Surface Texturing for the Intensification of Boiling Heat Transfer in a Minichannel

Kinga Strąk and Magdalena Piasecka *

Faculty of Mechatronics and Mechanical Engineering, Kielce University of Technology, 25-314 Kielce, Poland; kzietala@tu.kielce.pl
* Correspondence: tmpmj@tu.kielce.pl; Tel.: +48-41-34-24-320

Abstract: This study investigates the effects of using laser-textured surfaces in boiling heat transfer during cooling fluid flow in a minichannel. Several laser-textured surfaces, varied in roughness, were created on the heated plate surface that contacted FC-72 during flow in a single minichannel. Infrared thermography was used to measure temperature changes on the untextured side of the plate, while two-phase flow patterns were observed through a glass pane. Three vibration-assisted laser surface textures, previously investigated by the authors, and five novel laser surface textures were tested experimentally. The results were presented as relationships between heated wall temperature, heat transfer coefficient and distance along the minichannel, boiling curves, and flow patterns. The main interest of the authors was to provide a comparative analysis of the heat transfer results at the same value of heat flux supplied to the minichannel heated wall when either a laser-textured surface or a smooth base one was applied. It was noticed that the use of the 90-degree dense grid pattern type 2 (shallow) surface in the research helped achieve the highest local heat transfer coefficient in the subcooled boiling region compared to other surfaces tested. Furthermore, the 90-degree dense grid pattern type 1, characterised by larger maximum depth and height surfaces, performed best in the saturated boiling region. The results obtained for the laser-textured heated plate surface were compared to those collected for the smooth base heated plate surface, generally indicating an intensification of heat transfer processes in boiling heat transfer during FC-72 flow in a minichannel.

Keywords: laser surface; enhanced surface; flow boiling; heat transfer; minichannel; roughness

1. Introduction

Boiling heat transfer, a ubiquitous process in both industrial and domestic settings, can be significantly enhanced by modifying the heat transfer surface. This technique is particularly relevant in mini- and microchannel applications, driven by the ongoing trend of miniaturisation across various fields.

Researchers are exploring various techniques to optimise heat transfer performance, including geometric alterations, thermal flow adjustments, spatial reorientation, and surface modifications. One promising method involves laser texturing, which allows for precise control of surface properties such as roughness and wettability. By carefully adjusting the laser parameters, it is possible to create surfaces that promote efficient heat dissipation. The potential benefits of laser-textured surfaces in both pool and flow boiling are substantial. By altering the surface topography, researchers can enhance the density of the nucleation site, the diameter of bubble departure, and overall heat transfer coefficients. Collectively, these factors contribute to improved thermal performance [1].

A primary factor limiting industrial processes' efficiency is the heat removal rate. As a result, researchers continue to explore methods to enhance heat transfer. One particularly promising approach involves boiling heat transfer, which can be intensified through techniques such as nanofluids or textured surfaces.

In a recent study [2], researchers investigated the impact of nanosecond laser surface processing on the pool boiling heat transfer performance of copper surfaces under

atmospheric pressure and saturated conditions. Different surface textures were created by varying laser parameters such as wavelength (1064 nm, 355 nm, and 532 nm) and power.

The heat transfer coefficients of these laser-textured surfaces were compared to those of a smooth reference surface. Significant enhancements were observed: 93%, 62%, and 52% for the 1064 nm, 355 nm, and 532 nm wavelengths, respectively. These results highlight the potential of laser surface processing to significantly improve boiling heat transfer efficiency.

Another recent study [3] explored the influence of surface wettability and morphology on nucleate boiling heat transfer in laser-etched microchannels. The research focused on the interplay between these factors and their impact on boiling efficiency. Hydrophobic surfaces exhibited a strong correlation between the heat transfer coefficient (HTC) and the contact angle. Lower wettability led to higher HTC values. Conversely, hydrophilic surfaces showed a weak correlation, with increased critical heat flux (CHF) but lower HTC. The degree of laser texturing coverage significantly affected heat transfer performance. Higher coverage resulted in greater differences between the hydrophilic and hydrophobic surfaces. The study demonstrated that hydrophobized laser-textured surfaces offered the most significant improvement in HTC, achieving up to a 746% increase compared to untreated surfaces.

In reference [4], an intensification of heat transfer at low temperatures induced by water-repellent laser-textured surfaces on the inside of metal pipes was discussed. Using the laser surface texture of rough microgrooves, a superhydrophobic and water-repellent surface with a contact angle of 153° was obtained. Integration of the functionalised pipes in the condenser section of a two-phase closed thermosiphon showed a heat transfer rate of 0.92 kW at 45 °C and at 20 °C, with the respective heat sink temperature of the heat source at 20 °C. It was reported as approximately three times the heat transfer rate of 0.31 kW of a thermosiphon manufactured from a referenced smooth pipe.

Reference [5] presented an experimental study on the enhancement of nucleate boiling of Novec 649 on thin stainless-steel films with laser-induced periodic surface structures (LIPSS). The LIPSS samples featured microscale grooves with a depth of 19.6 μm and a width of 25 μm, leading to a 65% increase in the heat transfer coefficient (HTC) and a reduced wall superheat at the onset of boiling.

Submicroscale surface topography was identified as a critical factor in promoting boiling in dielectric applications.

In reference [6], the boiling characteristics of the R1234ze(E) working fluid were investigated on micro-textured surfaces created using laser interference structuring (LISS). These LISS-fabricated surfaces demonstrated a significant improvement in the maximum heat transfer coefficient, ranging from 240% to 275% compared to the untreated surface. However, a notable degradation in heat transfer was observed at higher heat fluxes.

One study [7] explored the enhancement of critical heat flux (CHF) in pool boiling of FC-72 under saturated and subcooled conditions using laser-textured stainless-steel surfaces combined with a hydrophobic coating. All enhanced surfaces demonstrated a significant increase in CHF, ranging from 36% to 73% at saturation and from 34% to 65% at 12 K subcooling.

Samples with laser-pretreated and hydrophobized spots exhibited the highest overall performance at saturation. However, a less steep CHF trend was observed with increasing liquid subcooling and increasing CHF with an increased superhydrophobic surface ratio.

In reference [8], 25 μm thick stainless-steel foils were used as heaters for pool boiling heat transfer experiments in both subcooled and saturated regions. Laser-textured areas were spaced apart by a capillary length of water (2.5 mm) and varied in arrangement and shape. The results indicated that all laser-textured boiling surfaces outperformed the base surface. The optimal distance between laser-textured areas was determined to be equal to the capillary length of the working fluid.

In the literature, there are many publications on flow boiling heat transfer in small channels with various modified surfaces: microfin and microcavity [9]; three fluorooctyl-trichlorosilane hydrophobic-patterned array structures having a triangle, inverted triangle,

and circular shape on a hydrophilic substrate [10]; CuO nanostructures created in the copper open microchannels [11]; a combination of interconnected microchannel net (IMN) and sintered porous material, with the porous interconnected microchannel net (PIMN) fabricated by solid-phase sintering and wire electric discharge machining with orthogonally interconnected microchannels [12]; porous [13,14]; and submillimetre/micro/nano-structured surfaces [15].

While laser-textured surfaces have been extensively studied for pool boiling heat transfer, their application to flow boiling heat transfer has received less attention.

The influence of wettability due to laser texture on the critical heat flux on flow boiling heat transfer in a vertical rectangular channel (heated from one side) was presented in [16]. The main section is a square channel with dimensions measuring 12.7 mm × 12.7 mm and a heated section 107.95 mm long. To change the wettability from hydrophilic to hydrophobic, surface texturing with a femtosecond laser was used. In experimental studies, the hydrophobic surface showed a delayed onset of boiling of the nuclei compared to the hydrophilic surface (boiling curves shifted toward higher wall superheating). Additionally, this surface resulted in a much lower CHF for the same system conditions and a lower sensitivity to changes in subcooling. In the study, surface preparation (mainly contact angle) had a significant impact on the CHF value and the ONB point.

Reference [17] presented a study on flow boiling heat transfer processes and pressure drop in rectangular minichannel heat sinks with and without artificial activation cavities by direct metal laser sintering. In the test section, R141b was used as a working fluid. The average heat transfer coefficients for minichannels with an artificial activation cavity were 2.03 to 2.62 times those of minichannels without an artificial activation cavity but under the same conditions.

Convective flow boiling heat transfer of R-134a on a bare aluminium surface and three microstructurally enhanced surfaces produced using photolithography and reactive ion etching techniques and by means of laser ablation was shown in [18]. In the results, the heat transfer coefficients on the surface made by the laser ablation process were up to 90–100% higher than the baseline surface. This phenomenon is attributed to the porous layer of sintered aluminium particles formed on the surface. Subsequently, the application of a hydrophobic coating to this surface resulted in a further increase in boiling heat transfer efficiency.

Nucleate flow boiling during the flow of FC-72 fluid in a closed-loop facility in porous metallic structures was presented in [19]. The porous surfaces were manufactured by the use of selective laser melting and exhibit an improved boiling heat transfer process compared to a plain surface. The authors stated that the reason for this is the increase in the number of nucleation sites and the more vigorous flow mixing. Initially, the heat transfer coefficient indicates an increasing trend from the low to mid-range of the exit vapour quality. Subsequently, as the dry-out condition approaches, it deteriorates afterwards.

Numerous articles focused on pool boiling heat transfer with the use of heaters (heated plates) with enhanced surfaces. Some examples are works authored by scientists from Kielce University of Technology [14,20–23]. The present article is a continuation of previous studies of the authors on flow boiling in minichannels using various enhanced heating surfaces, also produced with the help of several processes other than laser texturing, that is, the electro-machining process [24], emery paper-textured surfaces [25], and surfaces produced by soldering or sintering iron powder to the smooth plate base [25–29].

The main aim of the present study was to conduct an experimental investigation using enhanced heated surfaces produced by laser treatment and to analyse the results to identify an interesting solution for intensifying boiling heat transfer during flow in minichannels. It should be emphasised that the primary objective was to create new enhanced surfaces on the minichannel heated plate, but their geometric parameters were based on previous experiments after the results were analysed. These novel laser surfaces were produced using new advanced devices. The selection of enhanced surface geometries, i.e., modified surfaces due to laser texturing, was not random but was systematically based on previous

investigations. Furthermore, a larger number of enhanced surfaces were examined, and the most promising directions for development were selected for further analysis, with only the best-performing types being considered. In conclusion, the work focusses on a comparative analysis of laser-textured surfaces, including three previously studied vibration-assisted laser-textured surfaces and five novel laser surfaces. The primary objective was to identify the optimal laser-textured surface configuration to intensify heat transfer in flow boiling applications, especially for the construction of a minichannel compact heat exchanger.

2. Characteristics of the Laser Surface Texture Method

In this work, laser surface textures made on the base (smooth) surface are presented. A microstructure was formed on the surface used for laser processing, which was tested to verify whether heat transfer enhancement was achieved.

The smooth surface of the heated plate was made of Haynes-230 super alloy or Hastelloy X alloy, both manufactured by Haynes International, Inc. (Lenzburg, Switzerland).

Laser texturing is a micromachining technique that involves removing material using focused laser beam energy. By carefully controlling laser parameters such as intensity and exposure time [30], it is possible to create intricate surface structures with precise geometries and desired properties.

In the Haynes-230 alloy (with a thickness of approximately 0.45 mm), the main constituents include nickel–chromium–tungsten–molybdenum, in which the high nickel content provides a stable austenitic matrix, with the additions providing corrosion resistance, high temperature strength, and excellent long-term thermal stability [31]. The Hastelloy X alloy (with a thickness of approximately 0.65 mm) consists of a nickel–chromium–iron–molybdenum alloy and other additions. This alloy is characterised by high temperature strength, oxidation resistance, fabricability, and resistance to stress corrosion cracking [32].

In Table 1 are shown the main processing parameters of the produced laser surface textures: three vibration-assisted laser textures (VALS) and five novel laser ones (LS).

Each specimen with laser texture was placed in a selected area of dimensions: 180 mm × 16 mm. Three vibration-assisted laser textures (named #VALS1, #VALS2, and #VALS3) were produced using the CO_2 laser and a vibration exciter. In the study, the CO_2 Trumpf Lasercell 1005 and the laser/cutting head with a focal length of 200 mm were used, owned by the Centre for Laser Technologies of Metals, Kielce University of Technology.

Laser texturing offers enduring solutions for boiling surfaces by achieving specific surface roughness. By adjusting laser parameters, the surface morphology and thermophysical properties can be altered. This technique allows for the creation of boiling surfaces with excellent properties that intensify heat exchange. In laser texturing processes, the processed areas are in the order of micrometres or millimetres by removing the material using the laser beam energy. The material is processed to achieve the required geometry and/or distribution of properties. The aspect of beam pulse time is essential in laser microprocessing because it depends on radiation intensity and exposure time. The size of the heat zone depends on the duration of the pulse. It should be underlined that the improved laser texturing technique by inducing vibrations during the production of laser texture on the heated plate helps to intensify flow boiling heat transfer in minichannels, which was discussed in [33]. In this work, more detailed information on laser techniques was applied, and the research carried out previously by the authors is also reported.

The #VALS1 vibration-assisted laser surface texture was produced on the smooth surface of the heated plate made of Hastelloy X alloy. The processing parameters are listed in Table 1. The laser beam formed paths placed perpendicular to the fluid flow direction. On the melting area specimen (180 mm × 16 mm), 36 laser paths were produced, each of which had 3.8 mm width, were spaced 1.7 mm apart, and had 2.5 mm distance between the laser beam paths.

Table 1. The processing parameters of the laser surface textures.

Name of Laser Surface	The Basic Plate	Thickness of the Plate	Type of Laser	Laser Power	Other Properties
#VALS1	Hastelloy X	0.65 mm	CO_2 Trumpf Lasercell 1005, manufactured by Trumpf, Ditzingen, Germany, laser cutting, laser welding and tube cutting	2500 W	Scan velocity of 4 m/min Argon blow intensity of 10 l/min
#VALS2	Haynes-230	0.45 mm	CO_2 Trumpf Lasercell 1005, manufactured by Trumpf, Ditzingen, Germany, laser cutting, laser welding and tube cutting	1500 W	Scan velocity of 5 m/min Argon blow intensity of 10 l/min
#VALS3	Haynes-230	0.45 mm	CO_2 Trumpf Lasercell 1005, manufactured by Trumpf, Ditzingen, Germany, laser cutting, laser welding and tube cutting	1250 W	Scan velocity of 2.5 m/min Argon blow intensity of 10 l/min
#LS1	Haynes-230	0.45 mm	Fibre Laser 30 W, manufactured by Cormak, Siedlce, Poland, marking machine, laser engraver	30 W	Scan velocity of 100 mm/s wavelength of 1064 nm frequency of 20 KHz
#LS2	Haynes-230	0.45 mm	Fibre Laser 30 W, manufactured by Cormak, Siedlce, Poland, marking machine, laser engraver	30 W	Scan velocity of 100 mm/s wavelength of 1064 nm frequency of 20 KHz
#LS3	Haynes-230	0.45 mm	SPI 20 Laser, manufactured by SPI, Southampton, UK, single-mode, pulsed fibre lasers	20 W	Scanning velocity of 1 m/s Maximum pulse energy 0.8 mJ Pulse duration 200 ns frequency of 25 KHz
#LS4	Haynes-230	0.45 mm	SPI 20 Laser, manufactured by SPI, Southampton, UK, single-mode, pulsed fibre lasers	20 W	Scan velocity of 0.5 m/s Maximum pulse energy 0.8 mJ Pulse duration 200 ns frequency of 25 KHz
#LS5	Haynes-230	0.45 mm	SPI 20 Laser, manufactured by SPI, Southampton, UK, single-mode, pulsed fibre lasers	20 W	Scanning velocity of 1 m/s Maximum pulse energy 0.8 mJ Pulse duration 200 ns frequency of 25 KHz

Other vibration-assisted laser surface textures, named #VALS2 and #VALS3, were produced on a smooth heated plate surface made of the Haynes-230 alloy plate. In the case of these surfaces, the laser beam-formed paths on the specimens were consistent with the fluid flow direction. These laser textures were produced at the various parameters listed in Table 1. The vibration-assisted laser texture #VALS2 is a surface with cavities deeper and more widely spaced compared to #VALS1. Furthermore, the vibration-assisted laser texture named #VALS3 is characterised by more shallow cavities and overlapping tracks compared to the cavities produced in texture #VALS2.

The VALS textured surfaces were already studied by the authors in previously conducted research. Based on collected experimental data and the provided analysis of the results, it was found that the pattern development of the #VALS2 surface helps to intensify boiling heat transfer compared to the other surfaces tested. However, novel laser texturing on the heated plate has still been sought after. Therefore, proposals of new laser-textured surfaces were created. These were based on the assumption that surface development should not be too large but suitable enough with the aim of the heated plate laser-textured surface to support the initiation, development, and detachment of vapour bubbles during flow boiling in minichannels [29].

In addition to the vibration-assisted laser textures mentioned above, five novel laser surfaces (name LS) were also tested. Two of them, called #LS1 and #LS2, were produced

using a surface engraving machine—Fibre Laser 30 W, at an external company. Surface engraving was produced with an output wavelength of 1064 nm and a power of 30 W.

The following parameters were used for the process:

- Power of 100%;
- Speed of 100 mm/s;
- Number of passes: 1;
- Frequency of 20 kHz.

In #LS1 (60-degree line pattern), the laser paths were arranged at a 60 degree angle to the flow direction, spaced approximately 0.5 mm apart. In #LS2 (45-degree sparse grid pattern), laser paths were arranged at a 45-degree angle in two directions, intersecting to form rhombus shapes spaced approximately 1.5 mm apart. The specific parameters for each surface are detailed in Table 1.

Three other laser textures, namely #LS3, #LS4, and #LS5, were fabricated using an SPI 20 single-mode pulsed fibre laser at the Centre Laser Technologies of Metals, Kielce University of Technology. The laser parameters for these surfaces included the following:

- Maximum pulse energy of 0.8 mJ;
- Pulse duration 200 ns;
- Frequency of 25 kHz.

During the production process of surfaces #LS3 (45-degree dense grid pattern) and #LS5, a scanning velocity of 1 m/s was set. #LS4 had a scanning velocity of 0.5 m/s and a structure similar to #LS3, with laser paths forming diamond shapes. However, the path spacing was significantly denser, approximately 0.3 mm.

Both surfaces #LS4 (90-degree dense grid pattern type 1, deep) and #LS5 (90-degree dense grid pattern type 2, shallow) use a network of intersecting laser paths. These paths are perpendicular and parallel to the fluid flow, forming a grid-like pattern. While both surfaces share this basic design, #LS4's laser paths are etched deeper into the surface. (This pattern is characterised by larger depth and height of the maximum surface peak.)

Research of the roughness parameters of the vibration-assisted laser textures and laser surface texturing was conducted at the Kielce University of Technology. The geometric structures of the laser-modified surfaces were measured using a Leica DCM8 operating confocal microscope (Wetzlar, Germany). The Leica DCM8 is a 3D surface metrology microscope that combines high-definition confocal microscopy with interferometry. This dual-core system allows ultra-fast analysis with one-click mode selection, sophisticated software, and HD confocal scanning without moving parts.

The main parameters of the Leica DCM8 are as follows:

- Vertical resolution up to 0.1 nm with HD interferometry;
- Accuracy with open loop < 3% relative error and with closed loop < 20 nm error, for RGB HD true-colour imaging;
- Objectives from 1.25× up to 150× in confocal bright-field and dark-field modes, from 10× up to 50× in interferometry mode [25,34].

Views of the laser-modified surfaces of the heated plate, images of 3D topography of these surfaces, and the roughness profile of fragments of them are illustrated in Figures 1–4, respectively.

Figure 1 illustrates laser-modified heated plate surfaces: three vibration-assisted laser textures #VALS (Figure 1a–c) and five novel laser textures #LS (Figure 1d–h). For all surfaces tested, an identical fragment of the surface area was selected, with dimensions 2.5 mm by 3.0 mm. Analysing the data presented, it was found that the smallest surface development was obtained for two vibration-assisted laser textures (#VAL1, Figure 1a and #VAL2, Figure 1b) and two laser textures (#LS1, Figure 1d and #LS2, Figure 1e). Other tested surfaces, i.e., #VAL3 (Figure 1c), #LS3 (Figure 1f), #LS4 (Figure 1g), and #LS5 (Figure 1h), constituted a significant surface development, occupying more than half of the base sample.
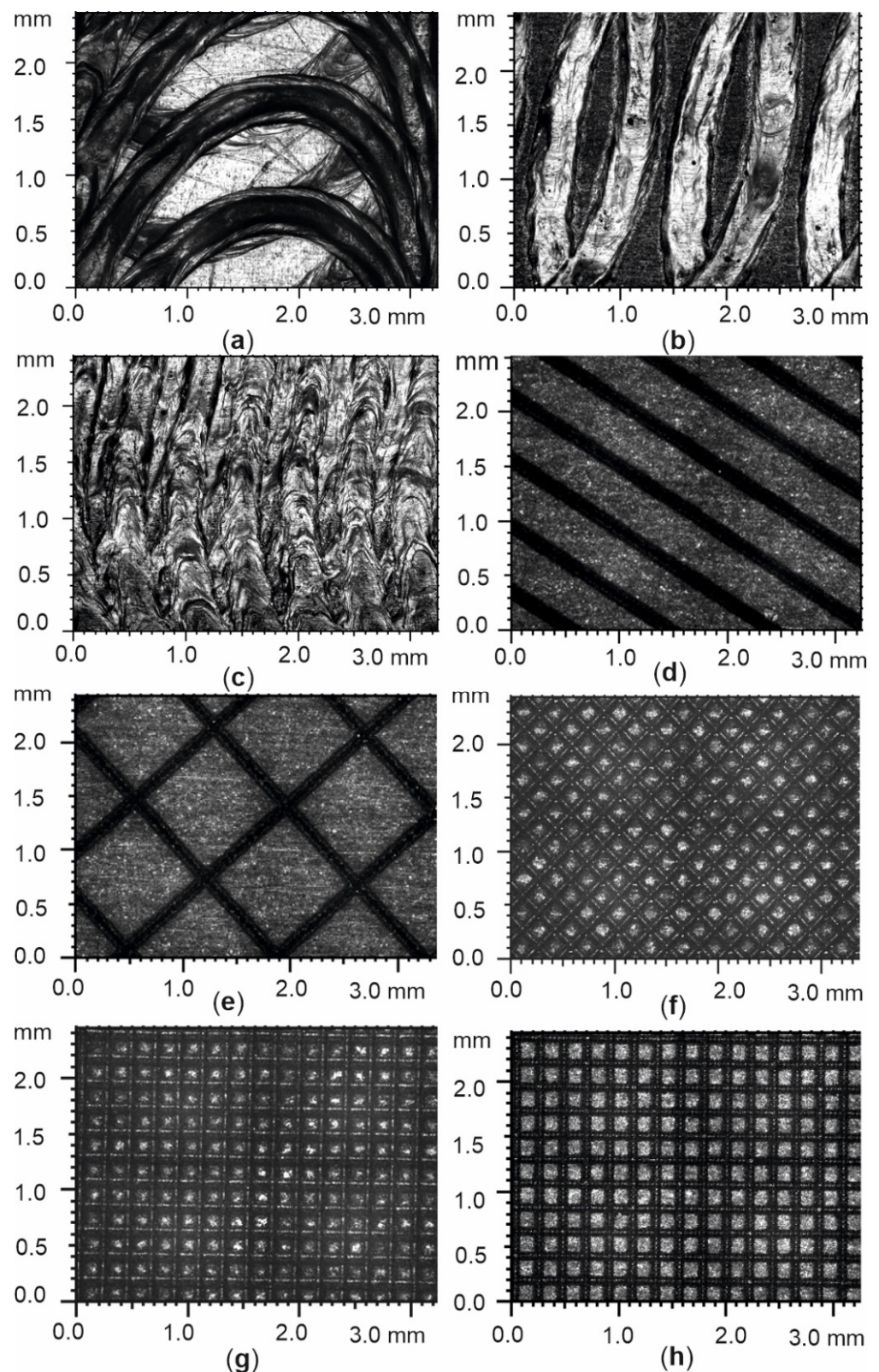
Figure 1. Views of laser-modified surfaces of the heated plate: (**a**–**c**) the vibration-assisted laser textures #VALS1 (**a**), #VALS2 (**b**), and #VALS3 (**c**); (**d**–**h**) the novel laser textures: 60-degree line pattern, #LS1 (**d**); 45-degree sparse grid pattern, #LS2 (**e**); 45-degree dense grid pattern, #LS3 (**f**); 90-degree dense grid pattern type 1, deep, #LS4 (**g**); and 90-degree dense grid pattern type 2, shallow, #LS5 (**h**).
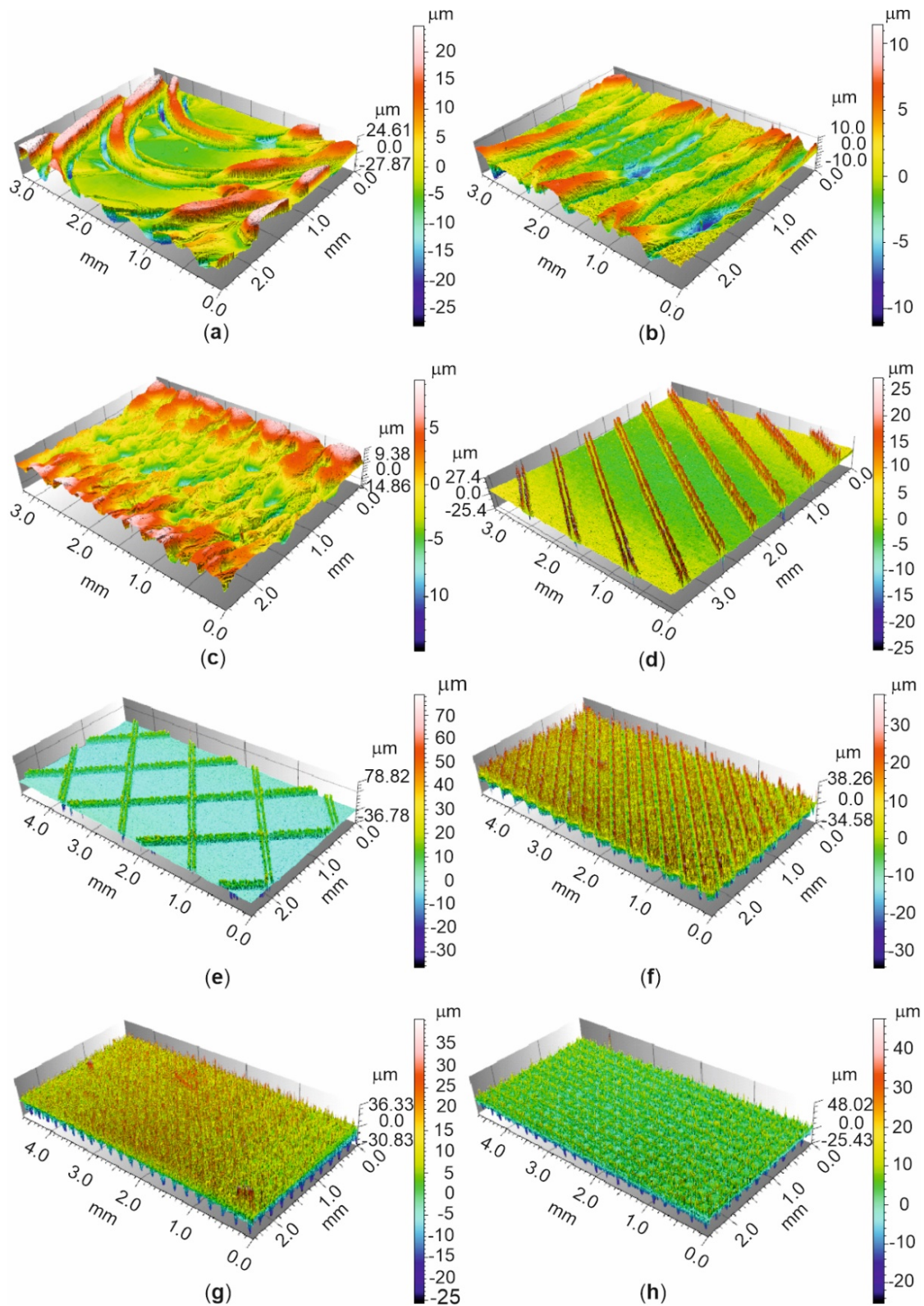
Figure 2. Three-dimensional topographies of laser-modified surfaces of the heated plate: (**a–c**) the vibration-assisted laser textures #VALS1 (**a**), #VALS2 (**b**), and #VALS3 (**c**); (**d–h**) the novel laser textures #LS1 (**d**), #LS2 (**e**), #LS3 (**f**), #LS4 (**g**), and #LS5 (**h**).
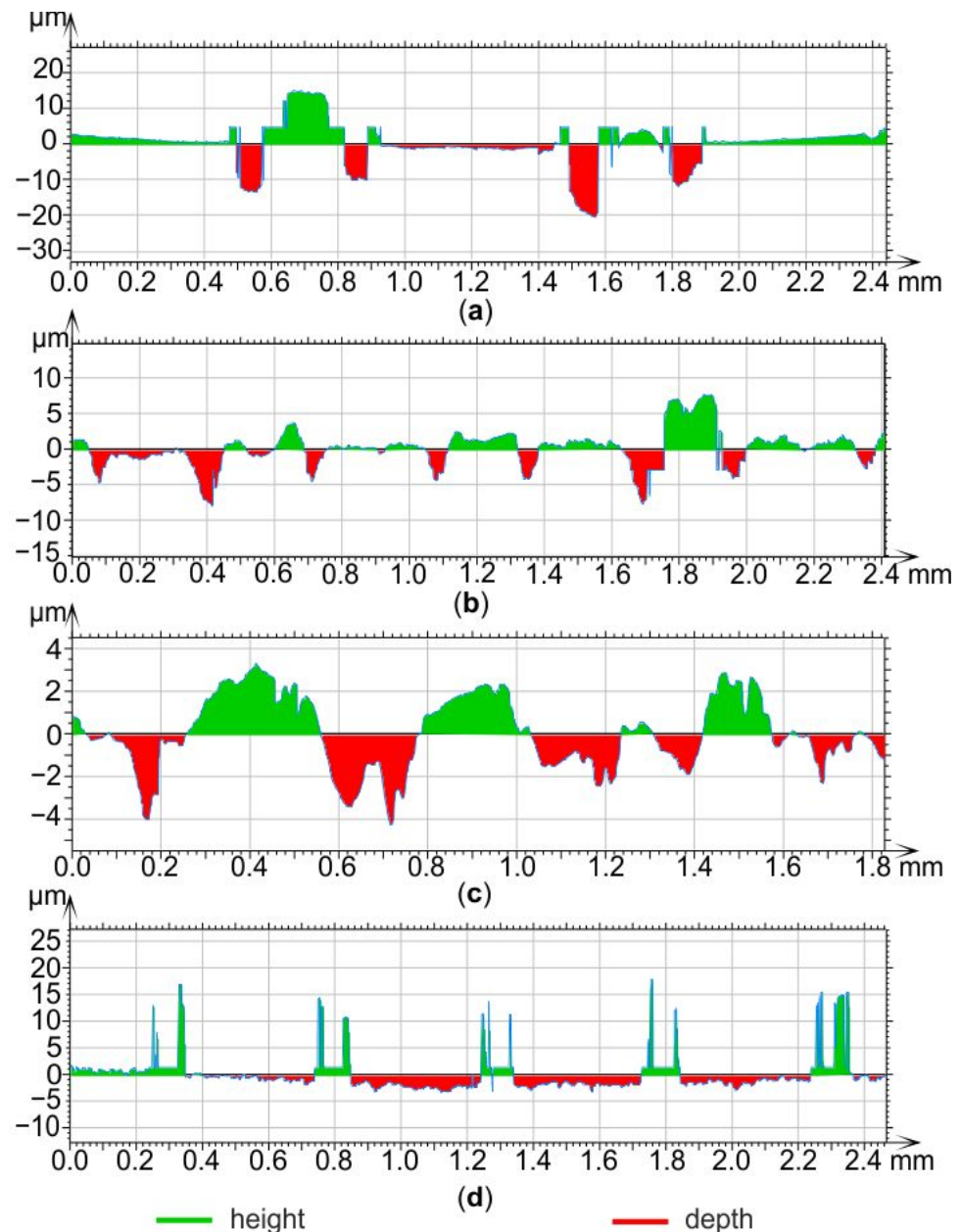
Figure 3. Roughness profiles of the fragment of laser-modified surfaces of the heated plate: (**a**–**c**) the vibration-assisted laser textures #VALS1 (**a**), #VALS2 (**b**), and #VALS3 (**c**,**d**); the novel laser texture #LS1.

The 3D topography images of all laser-modified surfaces of the heated plate are illustrated in Figure 2. A fragment of each enhanced heated plate surface of dimensions 2 mm × 3 mm (Figure 2a–c), 3 mm × 3 mm (Figure 2d), and 2 mm × 4 mm (Figure 2e–h) was selected. The largest cavities were observed for surface #LS2 (Figure 2e), while the smallest cavities were detected for surface #VALS2 (Figure 2b).

The roughness profile of each laser-modified heated plate surface fragment is shown in Figures 3 and 4. Roughness profiles were made in the central line of the heated plate test area, similar to the results in Figure 2.

The data captured for the laser modified surfaces #LS3 (Figure 4b), #LS4 (Figure 4c), and #LS5 (Figure 4d) were assumed to be the most developed, with a large number of peaks/depressions. However, it was observed that the least developed texture occurred on the surface #LS2 (Figure 4a).
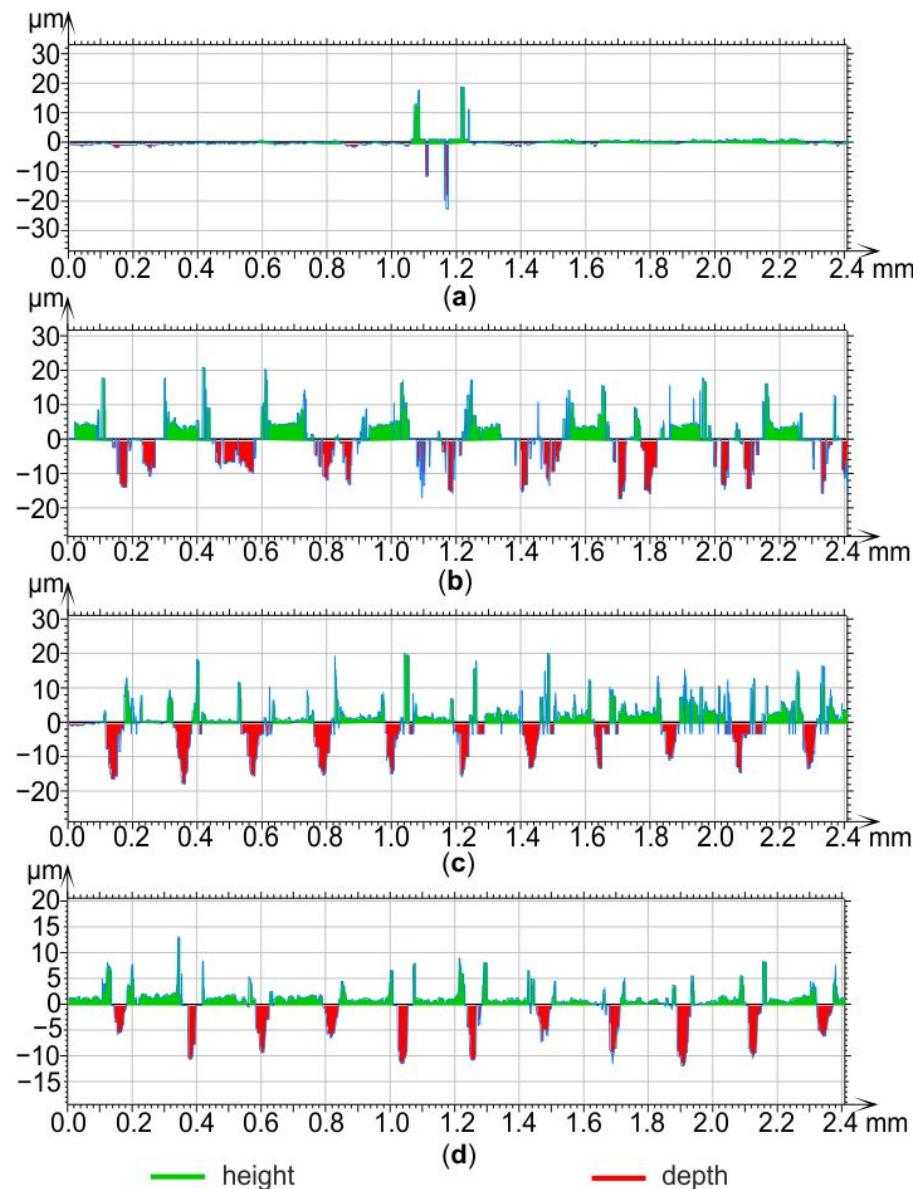
Figure 4. Roughness profile of the fragment of novel laser-textured surfaces of the heated plate: #LS2 (**a**), #LS3 (**b**), #LS4 (**c**), and #LS5 (**d**).

The maximum depth and height of all laser-modified surfaces tested are listed in Table 2.

Table 2. Maximum dimensions (depth and height) of the laser-modified surfaces.

Maximum Dimension [μm]	#VALS1	#VALS2	#VALS3	#LS1	#LS2	#LS3	#LS4	#LS5
Depth	20.73	7.985	4.272	3.347	22.57	17.32	17.76	12.02
Height	14.77	7.595	3.293	17.74	18.70	20.66	20.02	13.11

When analysing the data shown in Table 2, it was noted that maximum depth (22.57 μm, 17.32 μm, and 20.73 μm) and maximum height (18.70 μm, 20.66 μm, and 14.77 μm) were achieved for surfaces #LS2, #LS3, and #VAL1, respectively. However, the lowest values were noted for surface #VAL3 (max. depth 4.272 μm and max. height 3.293 μm).

In Table 3, profile roughness characteristics with roughness parameters, material ratio curves, roughness profile, and area roughness parameters of each laser-modified texture tested are reported.

Table 3. Roughness parameters of the laser-modified textures tested.

Roughness Parameter [Unit]	#VALS 1	#VALS 2	#VALS 3	#LS1	#LS2	#LS3	#LS4	#LS5
Profile roughness parameters								
Rp [μm]	9.958	4.989	2.517	16.17	17.71	18.99	19.57	8.611
Rv [μm]	16.01	7.436	3.658	2.303	12.31	17.33	15.55	11.34
Rz [μm]	25.96	12.37	6.175	18.47	30.02	36.33	35.11	19.95
Rc [μm]	16.41	7.589	4.523	12.52	25.02	26.06	18.43	12.93
Rt [μm]	28.52	14.29	6.175	20.58	41.29	37.82	35.94	20.41
Ra [μm]	4.834	2.040	1.445	1.578	0.9218	5.152	4.447	2.329
Rq [μm]	6.820	2.714	1.637	2.806	2.902	7.005	6.276	3.576
Rsk [-]	−0.8038	−0.6421	−0.1547	3.711	2.511	−0.1004	−0.1309	−1.464
Rku [-]	3.177	3.508	1.859	17.77	41.63	3.437	4.509	5.720
Material ratio of the profile and profile section height difference								
Rmr [%]	6.054	5.524	22.56	0.3300	0.7206	0.8006	1.601	0.7968
Rdc [μm]	8.391	4.222	3.012	1.240	1.026	10.98	6.861	1.732
Area roughness parameters								
Sq [μm]	9.234	3.503	3.134	3.903	5.187	8.523	7.314	5.401
Ssk [-]	0.3201	0.1661	0.0934	2.358	0.7284	−0.5675	−0.5935	−0.66
Sku [-]	3.338	3.574	2.677	13.25	13.50	5.478	4.300	5.046
Sp [μm]	24.61	16.11	9.381	27.43	78.82	38.26	36.33	48.02
Sv [μm]	27.87	15.84	14.86	25.42	36.78	34.58	30.83	25.43
Sz [μm]	52.48	31.95	24.24	52.85	115.6	72.85	67.16	73.44
Sa [μm]	6.658	2.769	2.511	2.326	2.693	5.496	5.022	3.654

where Rp—maximum height of the profile, Rv—maximum height of the profile, Rz—ten point height (deleted as an ISO parameter), Rc—mean height of the profile, Rt—total height of the profile, Ra—arithmetical mean deviation of the assessed profile, Rq—root mean square deviation of the assessed profile, Rsk—skewness of the assessed profile, Rku—kurtosis of the assessed profile, Rmr—material ratio of the profile, Rdc—profile section height difference, Sq—root mean square height, Ssk—skewness, Sku—kurtosis, Sp—maximum peak height, Sv—maximum pit height, Sz—maximum height, and Sa—arithmetical mean height.

According to the data presented in Table 3, it was observed that the highest values of the roughness parameters of the laser-textured surfaces tested were obtained for #LS3 and #VALS1 compared to the others. Specifically, Ra = 5.152 μm and Sa = 5.496 μm for surface #LS3, and Ra = 4.834 μm and Sa = 6.658 μm for surface #VALS1.

3. The Experimental Setup, Methodology, and Determination of the Heat Transfer Coefficient

3.1. Experimental Setup

Figure 5a demonstrates several systems performed on the experimental setup: Fluorinert FC-72 (3M) circulated in the main flow loop that included the test section. The power supply and control system, the data and image acquisition system, and the lighting system complemented the systems. All elements/devices of the experimental setup are listed in Table 4.

Figure 5b presents a view of the components of the test section. The vertical rectangular minichannel is placed between the glass plate and the heated plate. The depth of the minichannel results from the thickness of the fitted Teflon plate (22). A silicone O-ring is located in the grooves of the channel body (25) to prevent fluid leakage. A graphite plate (23) was applied to the electrical insulation metal elements of the test section. The test section is set vertically, with the working fluid flowing upward.
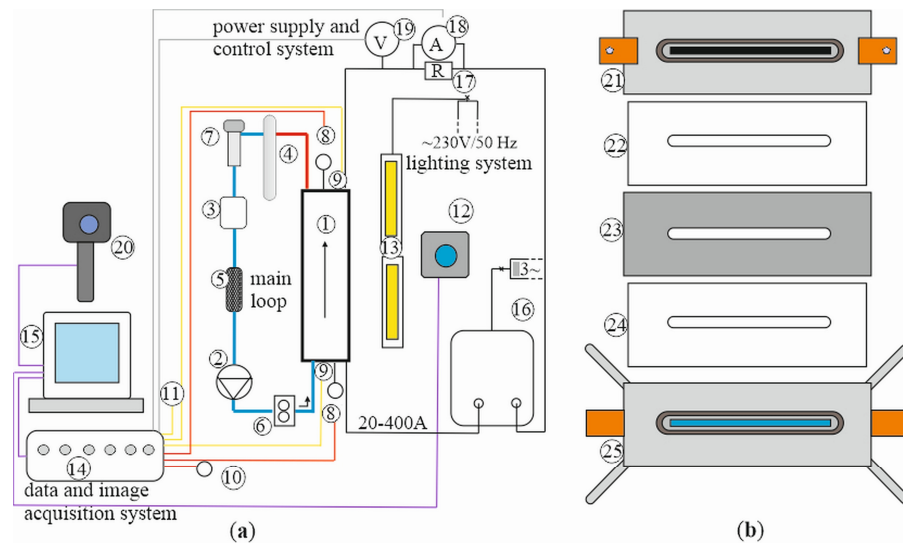
Figure 5. Schematic diagrams of (**a**) the experimental setup with the test section: 1—test section, 2—gear pump, 3—compensating tank, 4—heat exchanger, 5—filter, 6—mass flow meter, 7—deaerator, 8, 10—pressure meter, 9, 11—thermoelement, 12—high-speed digital camera, 13—LEDs, 14—data acquisition station, 15—PC computer, 16—inverter welder, 17—shunt, 18—ammeter, 19—voltmeter, and 20—IR camera; (**b**) view of the test section components: 21—a front cover, 22 and 24—a Teflon plate, 23—a graphite plate with enhanced heated plate, and 25—a channel body with an O-ring and glass plane.

Table 4. Elements/devices of the experimental setup.

Element/Device (Numbering, Figure 5a)	General Informations
Main Flow Loop	
Minichannel (1)	Single minichannel with dimensions: 180 mm in length and 1.7 mm in depth; set at the vertical position 90° with fluid upward flow
Gear circulating pump (2)	Model: SK 63 S/2 TF with Nordac SK 500E frequency inverter, manufactured by Nord Drivesystems, Stockholm, Sweden
Compensating tank (3)	Maintain the fluid pressure
Heat exchanger (4)	Type: pipe-in-pipe
Filter (5)	Solid–liquid separation
Coriolis mass flowmeter (6)	Model: Proline Promass A 100, manufactured by Endress+Hauser, Wroclaw, Poland
Deaerator (7)	Enables bleeding the systems
Pressure meters (8)	Model: PMP71 Cerabar S (overpressure at the inlet/outlet), manufactured by Endress+Hauser, Wroclaw, Poland
Thermocouples (9, 11)	K-type, 221 b, (9 at the inlet and outlet channel; 11 at ambient temperature), manufactured by Czaki Thermo-Product, Raszyn-Rybie, Poland
Pressure meter (10)	Model: A-10 (atmospheric pressure), manufactured by Wika, Klingenberg am Main, Germany
Power Supply and Control System	
PC computer (15)	Intel Core i9 CPU processor (24 cores), 3.50 GHz of clock speed, and 256 GB of RAM
Heat source (16)	Current regulation in the range 20–400 A
Shunt (17)	Model: 8B40-03, manufactured by Dataforth Corp., Tucson, AZ, USA
Ammeter (18)	Model: 8B32-01, manufactured by Dataforth Corp., Tucson, AZ, USA
Voltmeter (19)	Model: 8B41-12, manufactured by Dataforth Corp., Tucson, AZ, USA

Table 4. *Cont.*

Element/Device (Numbering, Figure 5a)	General Informations
	Data and Image Acquisition System
High-speed digital camera (12)	Model: SP-5000M-CXP2, the CoaXpress interface with two channels, manufactured by JAI Ltd., Yokohama, Kanagawa, Japan
Two data acquisition stations (14)	Model: DaqLab/2005 manufactured by IO-tech and model: MCC SC-1608G Series, manufactured by Measurement Computing, Norton, MA, USA
Infrared (IR) camera (20)	Model: E60, manufactured by FLIR Systems Inc., Wilsonville, OR, USA
	Lighting System
Leds (13)	8 high-power LED COB modules each with a power of 50 W

3.2. Experimental Methodology

The main measured data include thermograms on the minichannel heated plate (infrared thermography), as well as flow patterns (digital images in greyscale). Measurements were taken simultaneously from both sides of the test section: the infrared camera measured the temperature distribution on the outer (smooth) surface of the heated plate, while the high-speed digital camera recorded the flow pattern on the enhanced surface of the plate (at the opposite side of the test section).

The infrared camera self-calibrates once switched on, but it is necessary to set some parameters, such as the emissivity of the surface, the distance to the minichannel, and the relative humidity and temperature of the ambient air. For the high-speed digital camera, the distance from the test section, focus, and camera stability were adjusted.

Once the desired pressure and flow rate were reached, all of the following parameters were automatically recorded simultaneously:

- During 100 measurements, fluid temperatures at the inlet and outlet, ambient temperature, and atmospheric pressure were recorded and averaged using the DaqLab/2005 acquisition station in cooperation with DaqView version 9.1.35 software;
- The overpressure at both ends of the minichannel (inlet and outlet), the voltage drop, the current supplied to the heated wall, and the mass flow rate were measured 10 times each and averaged using the MCC SC-1608G series acquisition station and DaqView version 9.1.35 software;
- The heated wall temperature was captured using an infrared camera, and a linear temperature distribution along the channel's central axis was selected in the Researcher IR 4.0 programme.

During the experimental setup, the electric power supplied to the heated wall and the heat flux transferred to the fluid in the channel increased. Consequently, this led to the beginning of the onset of nucleate boiling and the heat transfer enhancement. Next, a further increase in the heat flux caused subcooled boiling (the liquid was superheated at the interface with the heated plate and subcooled at the core of the flow) and then started a saturated boiling region. After the maximum current was reached, there was a gradual decrease in the heat flux supplied to the heated wall. All tests were performed under stable thermal and flow conditions and steady-state regimes. The values or ranges of the experimental thermal and flow parameters are presented in Table 5.

Table 5. Experimental thermal and flow parameters.

Experimental Paramaters, (Unit)	Range of Values/Values
Inlet pressure, p_{in} (kPa)	125.9–175.1
Inlet liquid subcooling, ΔT_{sub} (°C)	49.9
Mass flux, G (kg/(m^2·s))	233.6
Heat flux, q_w (kW/m^2)	37.6–94.9

3.3. Heat Transfer Coefficient Determination

The heat transfer coefficient was calculated using the one-dimensional mathematical method based on one direction consistent with the depth of the minichannel and the thickness of the heated plate.

The local heat transfer coefficients $\alpha(x)$ in the subcooled and saturated boiling regions were determined from the following formula [29]:

$$\alpha(x) = \frac{q_w}{T_{IRT}(x, \delta_P) - T_f(x) - q_w \cdot \frac{\delta_P}{\lambda_{pP}}} \tag{1}$$

where

x—the distance from the minichannel inlet.

T_{IRT}—temperature of the heated plate measured by infrared thermography.

$T_f(x)$—local fluid temperature based on the assumption of linear distribution from the channel inlet to the outlet:

(i)   In the subcooled boiling region is the liquid bulk temperature (T_l);
(ii) In the saturated boiling region is the liquid saturated temperature (T_{sat}), both based on experimental measurements (of fluid temperature or pressure at the inlet and outlet, respectively).

δ_P—the heated plate thickness.

λ_P—the coefficient of thermal conductivity of the heated plate.

q_w—the heat flux transferred to the fluid in the minichannel.

The heat flux transferred to the fluid in the minichannel was estimated in Equation (2), as in [29]:

$$q_w = \frac{I \cdot \Delta U}{A} - q_{w,loss} \tag{2}$$

where

I—current supplied to the heated plate.

ΔU—voltage drop across the heated plate.

A—the surface area of the heated plate of the minichannel.

$q_{w,loss}$—heat loss to the surroundings.

The relative error of the heat flux (σ_{qw}) was calculated similarly to that of [25] for the subcooled boiling region and the lowest value of the heat flux taken into account in the error analysis; that is, q_w = 37.6 kW/m^2.

The mean relative error (σ_a) of the heat transfer coefficient was estimated similarly to [25] from the following formula:

$$\sigma_a = \frac{\sqrt{\left(\frac{\partial(x)}{\partial T_{IRT}(x)}\Delta T_{IRT}(x)\right)^2 + \left(\frac{\partial(x)}{\partial T_f(x)}\Delta T_f(x)\right)^2 + \left(\frac{\partial(x)}{\partial \lambda_P}\Delta \lambda_P\right)^2 + \left(\frac{\partial(x)}{\partial \delta_P}\Delta \delta_P\right)^2 + \left(\frac{\partial(x)}{\partial q_w}\Delta q_w\right)^2}}{\alpha(x)} \tag{3}$$

Furthermore, all components assumed in the calculation of the mean relative error of the heat transfer coefficient σ_a regarding the subcooled boiling region and the value of the heat flux q_w = 37.6 kW/m^2 are as follows:

- Plate temperature (measurement with an IR camera), $T_{IRT}(x)$ = 1.0 K;
- Fluid temperature (measurement by thermocouple), $\Delta T_f(x)$ = 0.34 K;
- Thermal conductivity of the heated plate (alloy Haynes-230), $\Delta \lambda_p$ = 0.1 W/(m·K);
- Thickness of the heated plate, $\Delta \delta_p$ = 5 × 10^{-5} m;
- Current supplied to the heated plate, ΔI = 0.18 A;
- Voltage drop across the heated plate, $\Delta(\Delta U)$ = 0.02 V;
- Area of the heated plate, ΔA = 2.8 × 10^{-5} m^2.

In [35], the assumptions and results of the statistical analysis are reported in detail.

In Table 6 are listed the relative errors of the heat flux (σ_{qw}) and the relative errors of the heat transfer coefficient (σ_a) at the subcooled boiling region for all enhanced heated plates with laser textures at the lowest heat flux equal to 37.6 kW/m^2.

Table 6. Relative errors of the heat flux and the heat transfer coefficient at subcooled boiling region for all laser textures tested.

Surface Textured	Heat Flux (kW/m^2)	σ_{qw} (%)	σ_a (%)
		Subcooled boiling region	
#VAL1		0.96	3.24
#VAL2		0.82	3.02
#VAL3		0.78	2.97
#LS1		0.78	3.49
#LS2	37.6	0.84	3.15
#LS3		0.84	2.99
#LS4		1.29	3.13
#LS5		1.27	4.69

When analysing the results listed in Table 6, it was noted that the relative error values (σ_{qw}) ranged from 0.78 to 1.29%. Furthermore, low values of relative errors of the heat transfer coefficient (σ_a) were achieved, ranging from 2.97% (for the laser surface # VAL3) to 4.69% (for the laser surface #LS5).

It should be explained that at the saturated boiling region, the measurement error value $T_{IRT} - T_{sat}$ occurs below 1 K. The authors assumed that, while the temperature difference error $T_{IRT} - T_{sat} < 1$ K, the data were not considered in the calculations, similarly to [36]. This assumption results directly from the relationship of temperature measurement errors with respect to the calculated temperature difference value, based on the data collected in experiments.

Generally, the results of the error analysis provided in this article confirm the previous results of the authors. It was observed that at subcooled boiling, the mean relative errors of the heat transfer coefficient achieved several per cent, but at saturated boiling, they are higher, reaching even 50%. According to [35], the mean relative errors of the heat transfer coefficient determined at subcooled boiling were in the range 3.14–5.02% and at saturated boiling were in the range 14.19–47.86%.

4. Results and Discussion

4.1. General Information

The experimental tests were carried out in steady state. The analysis presents data from the following:

- Smooth and various laser surface textures: three vibration-assisted laser-textured surfaces (#VALS1, #VALS2, and #VALS3) and five novel laser textures (#LS1, #LS2, #LS3, #LS4, and #LS5);
- Three heat fluxes transferred to the fluid in the minichannel: 37.6 kW /m^2, 48.5 kW/m^2, and 94.9 kW/m^2.

The results are presented graphically as follows:

- Plate temperature measurements using the IR camera vs. distance from the minichannel inlet (Figure 6);
- The heat transfer coefficient versus the distance from the minichannel inlet in two heat fluxes and at the subcooled boiling region, (Figure 7) and the saturated boiling region (Figure 8);
- Boiling curves: the relationship between the heat flux and the temperature difference between the heated wall and the fluid in the core (local values), generated for a 0.12 m distance from the minichannel inlet (Figure 9);

- Flow patterns—two phase flow structures captured for selected laser-textured surfaces: three vibration-assisted laser-textured surfaces, namely #VALS1, #VALS2, and #VALS3; laser texture #LS1 (Figure 10); and novel laser textures #LS2, #LS3, #LS4, and #LS5 (Figure 11).

4.2. Measured Temperature of the Heated Plate

Figure 6 shows the measured heated plate temperature vs. the distance from the minichannel inlet for three values for heat flux, i.e., 37.6 kW/m^2 (Figure 6a), 48.5 kW/m^2 (Figure 6b), and 94.9 kW/m^2 (Figure 6c), reported for the smooth and three vibration-assisted laser-textured surfaces (#VALS1, #VALS2, and #VALS3) and five novel laser surface textures (#LS1, #LS2, #LS3, #LS4, and #LS5). The temperature values of the heated plate were in a range from 307 to 360 K. The measured temperature values were observed to increase mainly with increasing distance from the minichannel inlet. It is obvious that the temperature achieved higher values with an increase in the heat flux transferred to the fluid flowing in the minichannel.
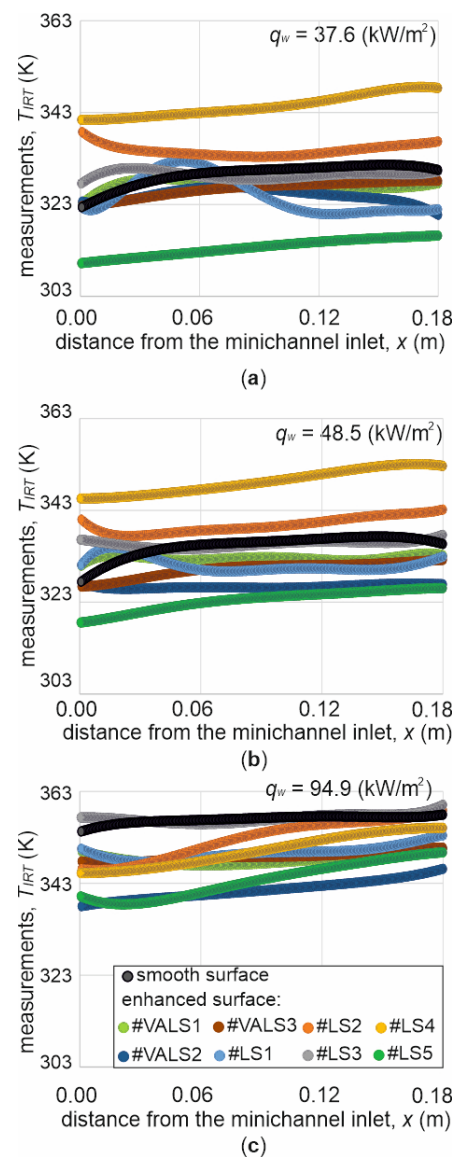

Figure 6. Plate temperature measurements (due to infrared thermography) versus distance from the minichannel inlet at three heat flux values transferred to the fluid in the minichannel: 37.6 kW/m^2 (**a**), 48.5 kW/m^2 (**b**), and 94.9 kW/m^2 (**c**).

4.3. Heat Transfer Coefficient

The heat transfer coefficient vs. distance values from the minichannel inlet collected for three heat fluxes when the smooth heated plate surface and eight laser-textured surfaces (vibration-assisted laser-textured and novel laser-textured surfaces) were applied in experiments and at similar experimental parameters are shown in Figures 7 and 8.

Furthermore, the results are reported separately for the two boiling regions of the subcooled boiling region (Figure 7) for two heat fluxes, namely 37.6 kW/m^2 (part a) and 48.5 kW/m^2 (part b), and the saturated boiling region (Figure 8), where two heat flux values were established: 48.5 kW/m^2 (part 'a') and 94.9 kW/m^2 (part 'b').
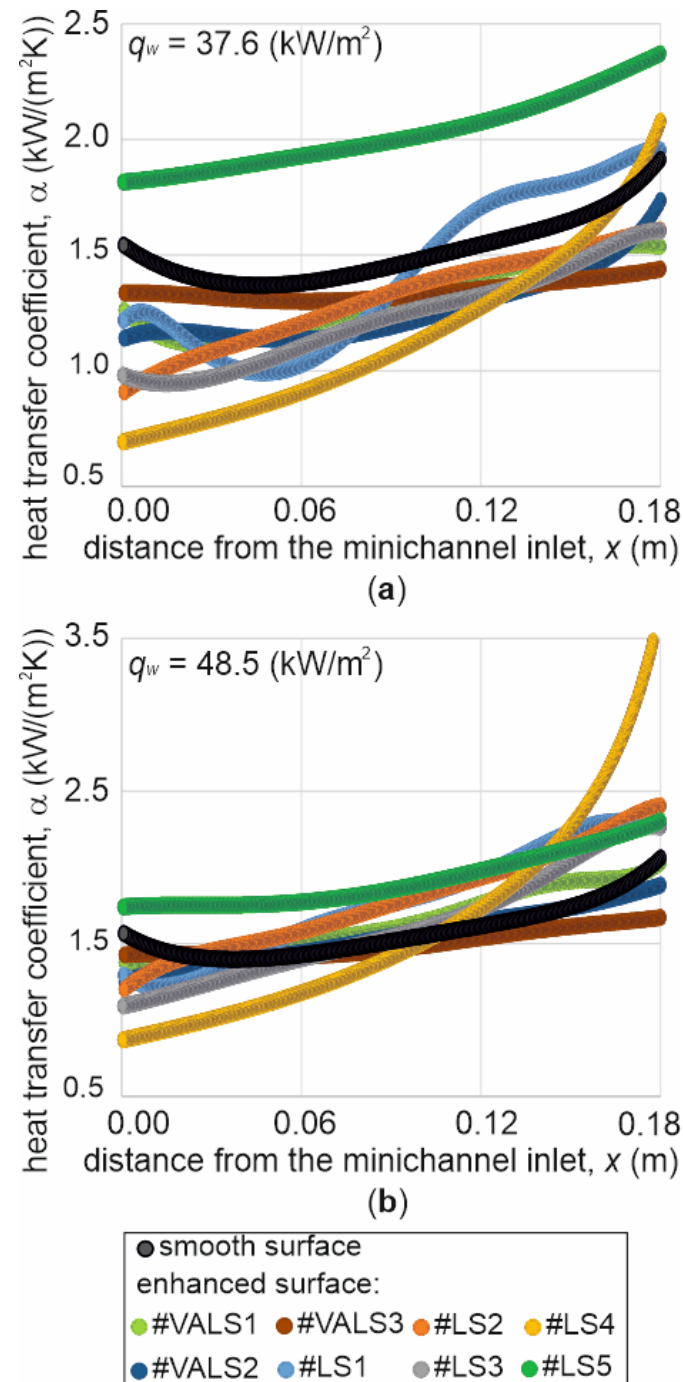
Figure 7. Heat transfer coefficient versus distance from the minichannel inlet in the subcooled boiling region and at two heat fluxes transferred to the fluid in the minichannel: 37.6 kW/m^2 (**a**) and 48.5 kW/m^2 (**b**).
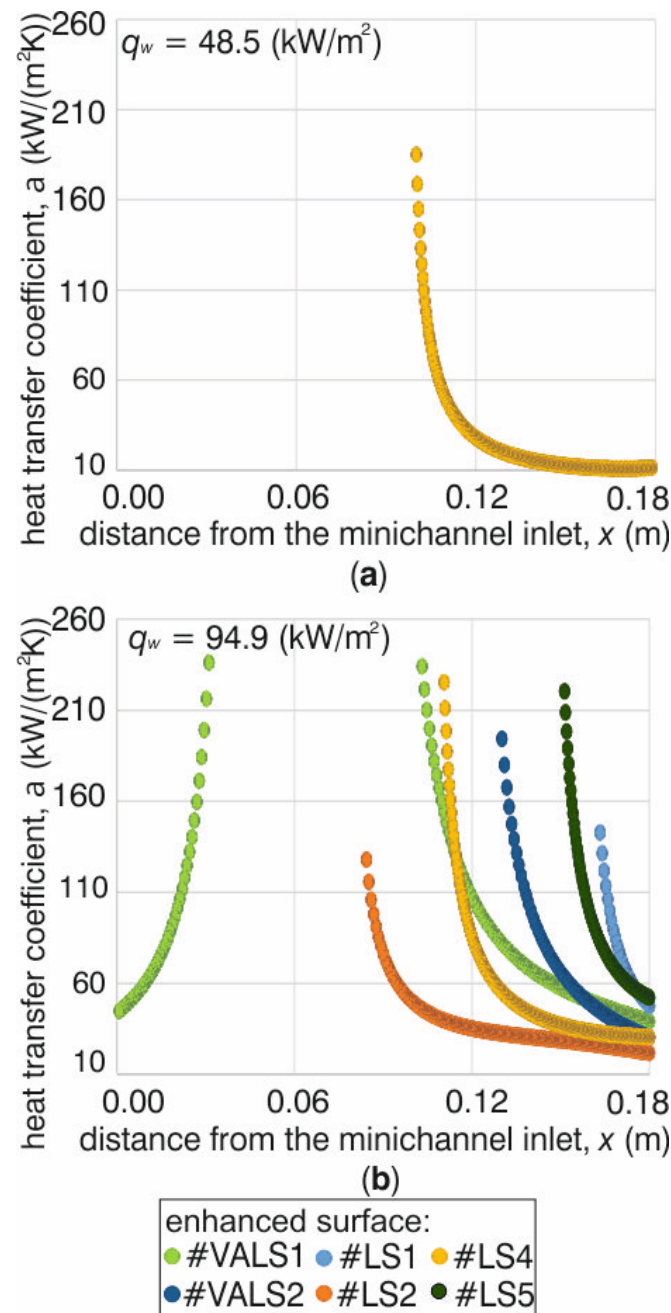
Figure 8. Heat transfer coefficient versus distance from the minichannel inlet for the saturated boiling region and at two heat fluxes transferred to the fluid in the minichannel: 48.5 kW/m^2 (**a**) and 94.9 kW/m^2 (**b**).

4.4. Analysis of Plate Temperature and Heat Transfer Coefficient Results

When analysing plate temperature results, it was also noted that the highest plate temperature was obtained for the novel laser surface texture #LS4 (90-degree dense grid pattern type 1, deep) at lower heat fluxes (Figure 6a,b), that is, at the subcooled boiling region. This laser surface texture is characterised by a larger maximum depth and height of the maximum surface peak. The opposite was observed in the heat transfer coefficient as a function of the distance from the minichannel inlet (Figure 7a,b) corresponding to the subcooled boiling region; that is, the lowest values of the heat transfer coefficient were found in the results collected for this texture at lower heat fluxes.

Furthermore, when analysing the data in Figure 6a,b, it is also clear that the lowest plate temperature occurred for the novel texture #LS5 in the subcooled boiling region,

corresponding to the achievement of the highest values of the heat transfer coefficient in this boiling region for this texture (Figure 7a,b). The #LS5 texture is a 90-degree dense grid pattern type 2 surface considered 'shallow' compared to #LS4 (which is characterised by a high depth and height of the maximum surface peak).

The authors' opinion is that too-deep cavities formed at the heated plate surface (as for texture #LS4) have a negative impact on its cooling during flow boiling. Deep cavities act as traps for vapour bubbles, delaying their spontaneous formation in the wall-adjacent layer and, subsequently, their detachment from the heated surface. The vapour bubbles act as heat sinks. With such an interpretation, the plate temperature of laser texture #LS4 achieved higher values compared to the other surfaces at the subcooled boiling region. Consequently, this phenomenon results in the achievement of lower values of the heat transfer coefficient in this region.

However, it was noticed that the use of the 90-degree dense grid pattern type 2 surface with shallower cavities (texture #LS5) helped achieve the lowest plate temperature (and the highest local heat transfer coefficient) in the subcooled boiling region compared to the other surfaces tested. This texture could support the occurrence of spontaneous formation in the adjacent wall layer. Shallower cavities could also help to tubulise the vapour bubbles and detach them from the heated plate surface. As a consequence, higher heat transfer coefficients can be obtained.

It could be added that the results collected for the highest heat flux are inconclusive (Figure 6c) because the data collected correspond to the transition from the subcooled region to the saturated one. At the highest heat flux, the highest plate temperature was recorded for the laser texture #LS3 (Figure 6c) and a smooth heated plate surface (Figure 6c). The lowest values of the measured temperature of the heated plate were captured for vibration-assisted laser-textured surfaces #VALS1 (Figure 6a,b) and #VALS2 (Figure 6c).

When analysing the results obtained in the subcooled boiling region (Figure 7), it was observed that the heat transfer coefficients increased with distance from the minichannel inlet for all heat fluxes and all types of heated plate surfaces contacting the fluid (smooth and enhanced by laser texturing processes). The coefficient values are approximately in the range from 0.7 to 3.5 kW/(m^2·K). The highest values were noted for the novel laser surface texture #LS5 (significantly, at the lowest heat flux of 37.6 kW/m^2, Figure 7a) and the novel laser texture #LS4 (only in the outlet part of the channel and at higher heat fluxes of 48.5 kW/m^2, Figure 7b). The lowest values of the coefficients were achieved for laser surface texture #LS4 in the inlet part of the channel. For all vibration-assisted laser surfaces, the textures had a slight increase in heat transfer coefficient along the entire length of the channel compared to all the laser-textured surfaces.

According to the results shown in Figure 8, referring to the saturated boiling region, it was observed that the heat transfer coefficients decreased mainly with increasing distance from the minichannel inlet for all enhanced surfaces and both heat fluxes. The heat transfer coefficients are in the range of approximately 10 to 230 kW/(m^2·K) and achieved much higher values compared to the values of the coefficients gained in the subcooled boiling region. It should be explained that it was possible to indicate the results at the saturated boiling region, which were collected under the same experimental conditions, only for enhanced surfaces, i.e., the two vibration-assisted laser surfaces (#VALS1 and #VALS2) and four novel laser surface textures (#LS1, #LS2, #LS4, and #LS5). The heat transfer coefficient for smooth surface #LS3 and for #VALS3 was not determined because the difference between the heated plate temperature and the fluid temperature (local values) was very small, close to the uncertainty of the temperature measurement.

Furthermore, the highest values of the heat transfer coefficient were observed for the novel laser texture #LS4 at both heat fluxes (heat transfer coefficient values at heat flux 48.5 kW/m^2 were obtained only for this surface, Figure 8a). In the saturated boiling region, deeper cavities characterised laser texture #LS4, which can support the mixing and tubulisation of the liquid–vapour mixture that flows in the channel, resulting in higher values of the heat transfer coefficient.

It was also noted that the heat transfer coefficient at a higher heat flux of 94.9 kW/m^2 achieved the highest values also for two enhanced surfaces #VALS and #LS5 (Figure 8b). Furthermore, at this heat flux (94.9 kW/m^2), the lowest coefficient values were found for the laser texture #LS2. In the developed boiling region, when the vapour share in the liquid–vapour mixture was dominant, the intensity of the heat transfer on flow boiling heat transfer also diminished.

The mean relative differences between the local temperature (measured due to infrared thermography) of the enhanced heated plate surface and temperature of the smooth one are determined from the flowing formula:

$$\varepsilon_{T,p} = \sum_{k=1}^{K} \frac{\left|T_{IRT,enhanced}(x_k) - T_{IRT,smooth}(x_k)\right|}{T_{IRT,smooth}(x_k)} \cdot \frac{100\%}{K} \ for \ k = 1\ldots K \tag{4}$$

where $T_{IRT,enhanced}$—local temperature measured due to infrared thermography for enhanced laser heated plate surface, $T_{IRT,smooth}$—local temperature measured due to infrared thermography for smooth heated plate surface, k—single point of the heated plate surface, and K—the total number of points of the heated plate surface.

The calculations were performed considering each laser plate surface and smooth surface for the selected values of heat flux considered in the subcooled boiling region. Data for the saturated boiling region were incomplete, which is why they were omitted from the analysis.

The mean relative differences between the local heat transfer coefficients gained from the calculations according to the 1D model in Equation (1) for the minichannel with each type of enhanced heated plate surface tested and the local heat transfer coefficients achieved under similar experimental conditions while mounted on a smooth heated plate surface were described as follows:

$$\varepsilon_{\alpha,p} = \sum_{k=1}^{K} \frac{\left|\alpha_{enhanced}(x_k) - \alpha_{smooth}(x_k)\right|}{\alpha_{smooth}(x_k)} \cdot \frac{100\%}{K} \ for \ k = 1\ldots K \tag{5}$$

where $\alpha_{enhanced}$—heat transfer coefficient determined for enhanced laser heated plate surface, α_{smooth}—heat transfer coefficient calculated for smooth heated plate surface, k—single point of the heated plate surface, and K—the total number of points of the heated plate surface.

In the calculations of $\varepsilon_{\alpha,p}$ according to Equation (5), each enhanced plate surface was considered in the analysis analogously to the case of determining the mean relative temperature differences determined from Equation (4).

The results of the calculations of mean relative differences for plate temperatures (Equation (4)) and heat transfer coefficients (Equation (5)) are summarised in Table 7.

Table 7. Mean relative differences between the temperatures or heat transfer coefficients of the enhanced and smooth heated plate surfaces used in experiments.

	$\varepsilon_{T,p}$ (%)		$\varepsilon_{\alpha,p}$	
Heat Flux (kW/m^2)	**37.6**	**48.5**	**37.6**	**48.5**
#VAL1	1.03	1.09	13.10	7.06
#VAL2	1.57	2.93	16.54	3.43
#VAL3	1.08	1.69	10.84	5.24
#LS1	1.90	1.70	14.51	18.18
#LS2	1.72	1.47	13.68	16.56
#LS3	0.74	0.48	17.68	9.52
#LS4	4.97	4.58	27.19	29.80
#LS5	5.33	3.91	33.94	23.82

When analysing the results shown in Table 7, it was noted that the maximum values of the mean relative differences between the local temperatures of the enhanced heated plate surfaces and a smooth surface were obtained for the following laser surfaces (at heat fluxes 37.6 kW/m^2 and 48.5 kW/m^2, respectively):

- #LS4: values of 4.97 and 4.58%;
- #LS5: values of 5.33 and 3.91%.

Other mean relative temperature differences were lower, reaching a maximum of 1.9% for the #LS1 laser surface at heat flux 37.6 kW/m^2.

Furthermore, the highest values of the mean relative differences between the local heat transfer coefficients for enhanced surfaces and the smooth surface were received for the subsequent laser surfaces (at heat fluxes 37.6 kW/m^2 and 48.5 kW/m^2, respectively):

- #LS4: values of 27.19 and 29.80%;
- #LS5: values of 33.94 and 23.82%.

Other mean relative heat transfer coefficient differences achieved lower values, while the lowest was obtained for #VAL surfaces at a higher heat flux (48.5 kW/m^2).

4.5. Boiling Curves

Figure 9 presents examples of boiling curves plotted for a selected point along the axis of the minichannel at a chosen distance from the inlet. Such curves describe that the heat flux density depends on the local heating surface or the temperature difference (local heated plate temperature minus local bulk fluid temperature).

The boiling curves were plotted for one cross-section of the minichannel along its central axis: 0.12 m—1/3 distance of the channel length from the channel outlet (Figure 9) for three vibration-assisted laser textures, namely #VALS1, #VALS2, and #VALS3 (Figure 9a), and the four laser surface textures, namely #LS1, #LS2, #LS3, #LS4, and #LS5 (Figure 9b).

It can be underlined that in this work, boiling curves represent the data collected during heat flux increase during the experiments. The first section of boiling curves (starting from the origin of the coordinate system) characterises the mechanism of single-phase forced convection (heat transfer proceeding between the heated plate and the working liquid). In the foil-adjacent area, the liquid becomes superheated, whereas in the flow core, it remains subcooled. The further increase in the heat flux results in the activation of the vapour nuclei along the heated plate surface. The boiling process starts and causes a sudden temperature drop (see the ONB point, which means the onset of nucleate boiling). Bubbles behave as internal heat sinks, absorbing internal energy and transferring it to the fluid. An increased heat flux leads to the transformation of the subcooled boiling region into the saturated boiling region.

The following observation can be drawn from the analysis of boiling curves in Figure 9: (i) generally, vibration-assisted laser textures represent a similar course of boiling curves, while ONB occurs at heat flux of 40 kW/m^2 (approximately), and (ii) the highest temperature drop during boiling incipience was observed for the #LS4 laser texture at a lower value of heat flux in comparison to the results at ONB when using vibration-assisted laser textures in research.

It could be emphasised that for the 90-degree dense grid pattern type 2 surface with shallower cavities, which helped achieve the lowest plate temperature (and the highest local heat transfer coefficient) in the subcooled boiling region, the highest values of temperature drop corresponding to boiling incipience occurred. As stated in previous subsection, this texture helps the spontaneous formation of the bubbles in the heated wall-adjacent layer. The bubbles function as internal heat sinks, absorbing a significant amount of energy transferred to the liquid and causing the highest temperature drop at ONB (Figure 9b).
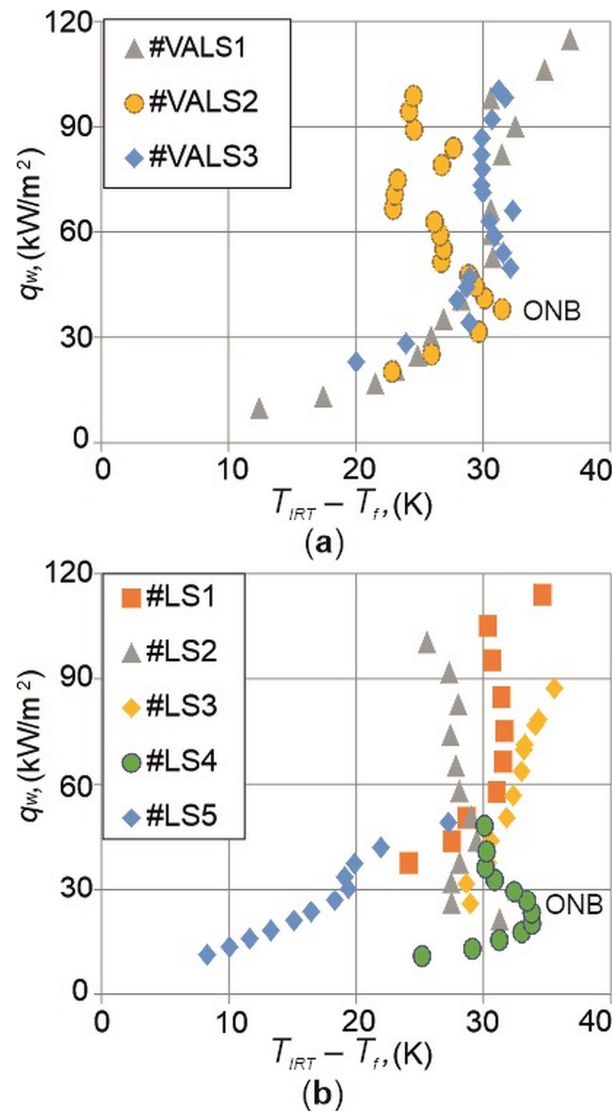
Figure 9. Boiling curves generated for 0.12 m distance from the minichannel inlet for laser-modified surfaces of the heated plate: the vibration-assisted laser textures #VALS1, #VALS2, and #VALS3 (**a**); and the laser textures #LS1, #LS2, #LS3, #LS4, and #LS5 (**b**). ONB—onset of nucleate boiling.

4.6. Flow Pattern

In Figures 10 and 11 are shown the flow patterns captured at the three flux values supplied to the heated plate (the same values chosen for data presented in Figure 7) and for various laser surface textures, such as the vibration-assisted laser surfaces #VALS1, #VALS2, and #VALS3 (Figure 10) and the laser surface textures #LS1 (Figure 10), #LS2, #LS3, #LS4, and #LS5 (Figure 11). In addition to all the images of the flow patterns, the enlarged fragments with characteristic structures and their magnification are marked in red lines in both figures.

It was observed that for all laser surfaces at two lower heat fluxes (named 1 and 2, Figures 10 and 11), only single vapour bubbles were observed in the outlet minichannel (except for the laser surface texture #LS4). For this texture (i.e., #LS4), larger vapour bubbles were visible at the minichannel inlet and near the side walls. Generally, the analysis of the flow structures for the highest heat fluxes (named 3, Figures 10 and 11) showed a bubblier structure in which tiny bubbles combined into larger groups, and significant amounts of the vapour phase were achieved in a two-phase mixture, mainly at the outlet of the minichannel. It should be mentioned that when analysing the flow pattern images of the laser surface texture #LS4, as illustrated in Figure 11, the highest vapour phase in

the two-phase mixture for all tested heat fluxes was compared to the other analysed laser structures (shown in Figures 10 and 11).
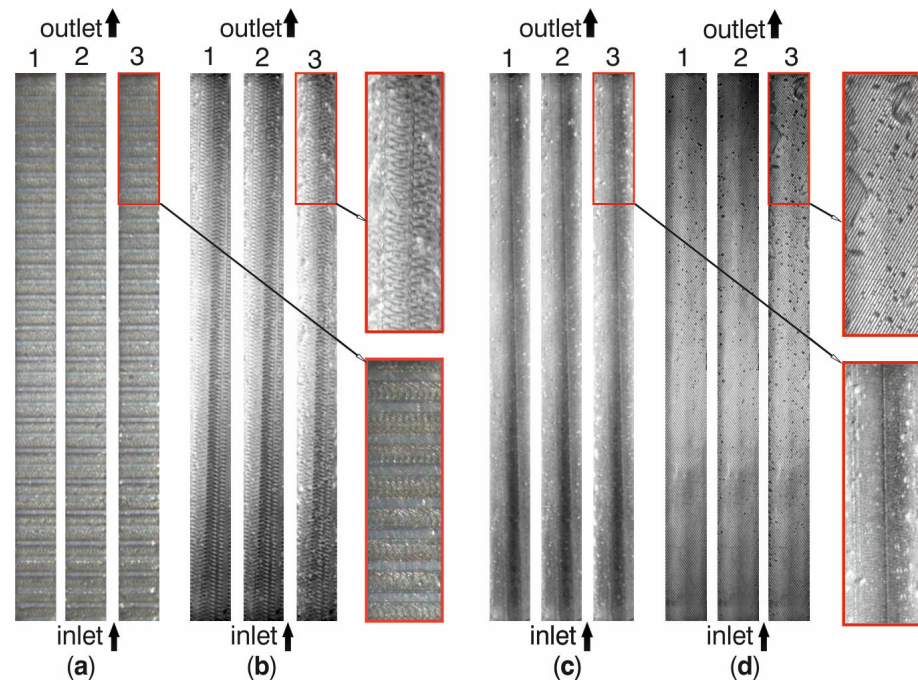

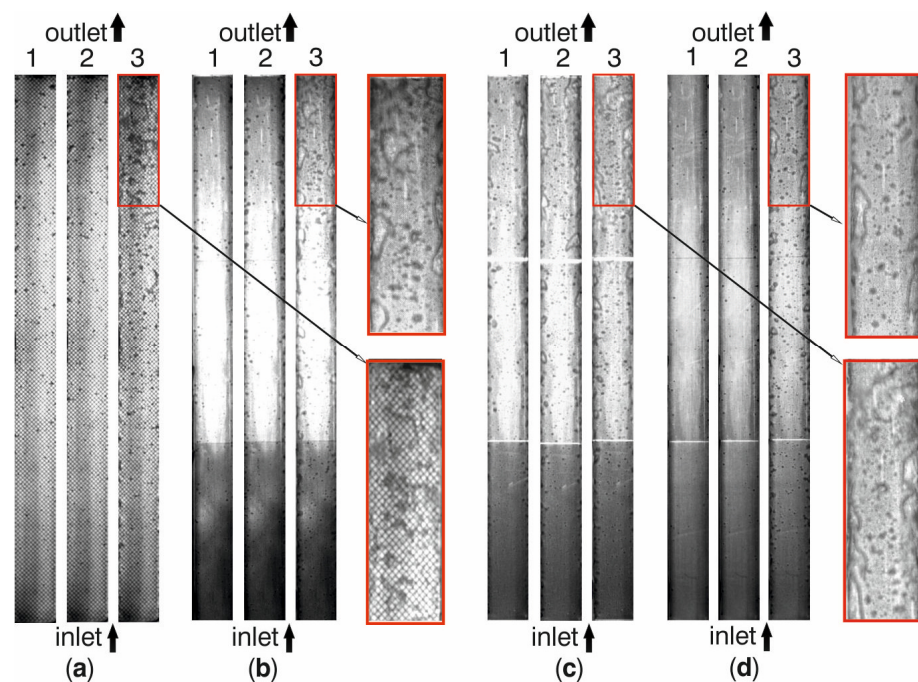**Figure 10.** Images of two-phase flow structures for three heat fluxes (the same as in Figure 6) and enhanced heated plate surfaces: the three vibration-assisted laser textures #VALS1 (**a**), #VALS2 (**b**), and #VALS3 (**c**) and the one selected laser texture #LS1 (**d**); the flow pattern with characteristic structures and its magnification are marked in red lines; 1, 2, 3—three values of increasing heat flux, with 1 representing the lowest.

Figure 11. Images of two-phase flow structures for three heat fluxes (the same as in Figure 6) and enhanced heated plate surfaces for the four laser textures #LS2 (**a**), #LS3 (**b**), #LS4 (**c**), and #LS5 (**d**); the flow patterns with characteristic structures and their magnification are marked in red lines; 1, 2, 3—three values of increasing heat flux, with 1 representing the lowest.

5. Conclusions

In the article, several laser-treatment-enhanced structures on a base smooth metal surface were tested in experiments. Two main groups were considered: vibration-assisted laser-textured surfaces (named VALS; three types) and laser-textured surfaces (named LS; five types). The main purpose of the study was to verify which of the enhanced surfaces tested helped to obtain a greater intensity of heat transfer during flow boiling in minichannels.

The geometric structure of the tested surfaces and methods of their production were herein presented. Various laser-textured surfaces were created and used to study the boiling heat transfer during the Fluorinert FC-72 flow in a single minichannel heat exchanger. Infrared thermography was used to measure the changes in temperature on the smooth outer surface of the heated plate, while two-phase flow patterns were observed through a glass pane. The experimental results are shown as the relationships between the heated wall temperature and the heat transfer coefficient and the distance along the length of the minichannel for the two boiling regions, namely subcooled and saturated, along with boiling curves and images of flow patterns.

The main findings of the study are as follows:

- Among all enhanced surfaces tested, the highest values of surface texture dimensions (maximum depth and maximum height) were observed for the novel laser texture named #LS3 (45-degree dense grid pattern) and one of the vibration-assisted laser textures tested in previous investigations by the authors (#VALS1);
- Regarding heat transfer intensification, the enhanced structures of the LS (novel laser textures) and VALS surfaces (the vibration-assisted laser textures) outperformed the base smooth sample;
- The highest plate temperature was recorded for the two novel laser-textured surfaces #LS4 and #LS3 and the smooth heated plate surface. Conversely, the lowest temperatures were observed for the two vibration-assisted laser-textured surfaces #VALS1 and #VALS2;
- The highest local heat transfer coefficient was achieved by the novel laser texture #LS5 (90-degree dense grid pattern type 2, shallow) at the subcooled boiling region and by the novel laser texture #LS4 (90-degree dense grid pattern type 1, deep—pattern with larger maximum depth and height) at the saturated boiling region, outperforming other surfaces at similar heat fluxes;
- Vibration-assisted laser textures represent a similar course of boiling curves, while the onset of nucleate boiling (ONB) occurred at a constant heat flux; the highest temperature drop during boiling incipience was observed for the novel laser texture #LS4 at a lower value of heat flux in comparison to the ONB results obtained using vibration-assisted laser textures in research;
- The highest phase fraction in the two-phase mixture was observed for the laser-textured surface #LS4 (at all selected heat fluxes) compared to other laser structures.

Based on these findings, the laser-textured surface #LS4 (90-degree dense grid pattern type 1, deep, i.e., with larger maximum depth and height) appears to be the most promising for achieving significant heat transfer intensification. Future research will explore the performance of this surface under different test and work conditions. This novel surface is indicated for further studies on heat transfer during the flow of working fluids through a group of minichannels in a solar collector.

Laser-treated surfaces are beneficial for improving heat transfer during flow boiling because they can increase active surface area, surface roughness, wettability, and absorption capacity. These laser-texturing techniques are easy to apply, flexible, and cost-effective and provide durable surface structures. Two novel laser textures (90-degree dense grid patterns: deep and shallow) are planned for use in further flow boiling heat transfer research depending on the type of boiling regions (subcooled or saturated) in a minichannel solar collector.

Nomenclature

A	channel cross-sectional area, m^2
a_s	heat transfer coefficient between the heated plate and surroundings, W/(m^2·K)
G	mass flux, kg/(m^2·s)
I	current, A
p	pressure, Pa
q	heat flux, W/m^2
T	temperature, K
x	distance from the minichannel inlet, m
Greek Symbols	
α	heat transfer coefficient between the heated plate and the working fluid flowing in the central minichannel, W/(m^2·K)
δ	thickness, m
ε	mean relative difference
λ	thermal conductivity, W/(m·K)
σ	mean relative error of the heat transfer coefficient
ΔU	voltage drop, V
Subscripts	
f	fluid
l	liquid
in	at the inlet
IRT	infrared
$loss$	heat loss
out	at the outlet
P	plate
sat	saturation

References

1. Udaya Kumar, G.; Suresh, S.; Sujith Kumar, C.S.; Back, S.; Kang, B.; Lee, H.J. A review on the role of laser textured surfaces on boiling heat transfer. *Appl. Therm. Eng.* **2020**, *174*, 115274. [CrossRef]
2. Nirgude, V.V.; Sahu, S.K. Heat transfer enhancement in nucleate pool boiling using laser processed surfaces: Effect of laser wavelength and power variation. *Thermochim. Acta* **2020**, *694*, 178788. [CrossRef]
3. Žalec, D.; Može, M.; Zupančič, M.; Golobič, I. Elucidating the effects of surface wettability on boiling heat transfer using hydrophilic and hydrophobic surfaces with laser-etched microchannels. *Case Stud. Therm. Eng.* **2024**, *57*, 104357. [CrossRef]
4. Holder, D.; Peter, A.; Kirsch, M.; Cáceres, S.; Weber, R.; Onuseit, V.; Kulenovic, R.; Starflinger, J.; Graf, T. Enhancing heat transfer at low temperatures by laser functionalization of the inner surface of metal pipes. *Sci. Rep.* **2024**, *14*, 2557. [CrossRef] [PubMed]
5. Zupančič, M.; Fontanarosa, D.; Može, M.; Bucci, M.; Vodopivec, M.; Nagarajan, B.; Vetrano, M.R.; Castagne, S.; Golobič, I. Enhanced nucleate boiling of Novec 649 on thin metal foils via laser-induced periodic surface structures. *Appl. Therm. Eng.* **2024**, *236*, 121803. [CrossRef]
6. Hirahara, H.; Motomura, F.; Liu, Y.; Kondou, C. Heat transfer enhancement of aluminum boiling surface with micro-grooves fabricated by laser. *Int. J. Thermofluids* **2023**, *17*, 100274. [CrossRef]
7. Ferjančič, K.; Može, M.; Križan, P.; Bobič, M.; Golobič, I. Subcooled critical heat flux on laser-textured stainless-steel ribbon heaters in pool boiling of FC-72. *Int. J. Heat Mass Transf.* **2020**, *159*, 120090. [CrossRef]
8. Voglar, J.; Gregorčič, P.; Zupančič, M.; Golobič, I. Boiling performance on surfaces with capillary-length-spaced one- and two-dimensional laser-textured patterns. *Int. J. Heat Mass Transf.* **2018**, *127*, 1188–1196. [CrossRef]

9.   Lin, Y.; Luo, Y.; Wang, E.N.; Li, W.; Minkowycz, W.J. Enhancement of flow boiling heat transfer in microchannel using micro-fin and micro-cavity surfaces. *Int. J. Heat Mass Transf.* **2021**, *179*, 121739. [CrossRef]

10.   Hsu, W.T.; Lee, D.; Lee, N.; Yun, M.; Cho, H.H. Enhancement of flow boiling heat transfer using heterogeneous wettability patterned surfaces with varying inter-spacing. *Int. J. Heat Mass Transf.* **2021**, *164*, 120596. [CrossRef]

11.   Yin, L.; Yang, Z.; Zhang, K.; Xue, Y.; Dang, C. Heat Transfer of Water Flow Boiling in Nanostructured Open Microchannels. *Energies* **2023**, *16*, 1303. [CrossRef]

12.   Chen, J.; Zhang, S.; Tang, Y.; Chen, H.; Yuan, W.; Zeng, J. Effect of operational parameters on flow boiling heat transfer performance for porous interconnected microchannel nets. *Appl. Therm. Eng.* **2017**, *121*, 443–453. [CrossRef]

13.   Lee, V.Y.S.; Henderson, G.; Reip, A.; Karayiannis, T.G. Flow boiling characteristics in plain and porous coated microchannel heat sinks. *Int. J. Heat Mass Transf.* **2022**, *183*, 122152. [CrossRef]

14.   Orman, Ł.J. Enhanced boiling heat transfer on surfaces covered with microstructural mesh coatings. *Jordan J. Mech. Ind. Eng.* **2019**, *13*, 155–160.

15.   Huang, S.; Wang, L.; Pan, Z.; Zhou, Z. Experimental investigation of a new hybrid structured surface for subcooled flow boiling heat transfer enhancement. *Appl. Therm. Eng.* **2021**, *192*, 116929. [CrossRef]

16.   Bottini, J.L.; Kumar, V.; Hammouti, S.; Ruzic, D.; Brooks, C.S. Influence of wettability due to laser-texturing on critical heat flux in vertical flow boiling. *Int. J. Heat Mass Transf.* **2018**, *127*, 806–817. [CrossRef]

17.   Zhou, J.; Luo, X.; Pan, Y.; Wang, D.; Xiao, J.; Zhang, J.; He, B. Flow boiling heat transfer coefficient and pressure drop in minichannels with artificial activation cavities by direct metal laser sintering. *Appl. Therm. Eng.* **2019**, *160*, 113837. [CrossRef]

18.   Sommers, A.D.; Yerkes, K.L. Using micro-structural surface features to enhance the convective flow boiling heat transfer of R-134a on aluminum. *Int. J. Heat Mass Transf.* **2013**, *64*, 1053–1063. [CrossRef]

19.   Wong, K.K.; Leong, K.C. Nucleate flow boiling enhancement on engineered three-dimensional porous metallic structures in FC-72. *Appl. Therm. Eng.* **2019**, *159*, 113846. [CrossRef]

20.   Hożejowska, S.; Kaniowski, R.; Pastuszko, R. Application of the Trefftz Method for Pool Boiling Heat Transfer on Open Microchannel Surfaces. *Heat Transf. Eng.* **2022**, *43*, 362–370. [CrossRef]

21.   Kaniowski, R.; Pastuszko, R. Pool boiling experiment with Novec-649 in microchannels for heat flux prediction. *Exp. Therm. Fluid Sci.* **2023**, *141*, 110802. [CrossRef]

22.   Orman, Ł.J.; Radek, N.; Pietraszek, J.; Wojtkowiak, J.; Szczepaniak, M. Laser Treatment of Surfaces for Pool Boiling Heat Transfer Enhancement. *Materials* **2023**, *16*, 1365. [CrossRef] [PubMed]

23.   Orman, Ł.J.; Radek, N.; Pietraszek, J.; Szczepaniak, M. Analysis of enhanced pool boiling heat transfer on laser-textured surfaces. *Energies* **2020**, *13*, 2700. [CrossRef]

24.   Strąk, K.; Piasecka, M. Boiling heat transfer during flow of distilled water in an asymmetrically heated rectangular minichannel. *EPJ Web Conf.* **2017**, *143*, 02116. [CrossRef]

25.   Piasecka, M.; Strąk, K. Boiling Heat Transfer during Flow in Vertical Mini-Channels with a Modified Heated Surface. *Energies* **2022**, *15*, 7050. [CrossRef]

26.   Depczyński, W.; Piasecki, A.; Piasecka, M.; Strąk, K. Impact of Fe powder sintering and soldering in production of porous heating surface on flow boiling heat transfer in minichannels. *E3S Web Conf.* **2017**, *19*, 03012. [CrossRef]

27.   Piasecka, M.; Strąk, K. Influence of the Surface Enhancement on the Flow Boiling Heat Transfer in a Minichannel. *Heat Transf. Eng.* **2019**, *40*, 1162–1175. [CrossRef]

28.   Maciejewska, B.; Strak, K.; Piasecka, M. The solution of a two-dimensional inverse heat transfer problem using two methods: The Trefftz method and the Beck method. *Int. J. Numer. Methods Heat Fluid Flow* **2018**, *28*, 206–219. [CrossRef]

29.   Piasecka, M.; Strąk, K. Characteristics of Refrigerant Boiling Heat Transfer in Rectangular Mini-Channels during Various Flow Orientations. *Energies* **2021**, *14*, 4891. [CrossRef]

30.   Grabas, B. Impact of the Parameters of Laser-Vibration Treatment on the Roughness of Aluminium Melts. *Adv. Mater. Res.* **2014**, *874*, 71–75. [CrossRef]

31.   HAYNES® 230® Alloy Information. Available online: http://www.haynesintl.com (accessed on 13 May 2024).

32.   Haynes International, Inc. Hastelloy X Alloy (Product Brochure) Information. 1997. Available online: http://www.haynes.ch (accessed on 13 May 2024).

33.   Piasecka, M.; Strąk, K.; Grabas, B. Vibration-assisted laser surface texturing and electromachining for the intensification of boiling heat transfer in a minichannel. *Arch. Metall. Mater.* **2017**, *62*, 1983–1990. [CrossRef]

34.   Available online: https://www.leica-microsystems.com/products/digital-microscopes/p/leica-dcm8/ (accessed on 17 July 2024).

35.   Piasecka, M.; Strąk, K.; Maciejewska, B. Heat transfer characteristics during flow along horizontal and vertical minichannels. *Int. J. Multiph. Flow* **2021**, *137*, 103559. [CrossRef]

36.   Strak, K.; Maciejewska, B.; Piasecka, M. The heat transfer coefficient determination with the use of the Beck-Trefftz method in flow boiling in a minichannel. *EPJ Web Conf.* **2018**, *180*, 02099. [CrossRef]